Supplementary Information

Ultralight and Robust Carbon Nanofiber Aerogel for Advanced Energy Storage

Yu Ma,†[a,b] Qiao Liu,†[b] Weijun Li,[b] Yapeng Zheng,[b] Qing Shi,[b] Zeyan Zhou,[a] Gang Shao,[d] Weiyou Yang,*[b] Ding Chen,*[a,c] and Xiaosheng Fang *[e]

[a] College of Materials Science and Engineering, Hunan University, Changsha 410082, P.R. China.

[b] Institute of Materials, Ningbo University of Technology, Ningbo City 315016, P.R. China.

[c] State Key Laboratory of Advanced Design and Manufacturing for Vehicle Body, Hunan University, Changsha 410082, P.R. China.

[d] School of Materials Science and Engineering, Zhengzhou University, Zhengzhou 450001, P.R. China.

[e] Department of Materials Science, Fudan University, Shanghai, 200433, P. R. China.

† Yu Ma and Qiao Liu contributed equally to the present work.

E-mails: chending@hnu.edu.cn (D. Chen)
weiyouyang@tsinghua.org.cn (W. Yang)
xshfang@fudan.edu.cn (X. Fang)

Experimental Section

Materials and Chemicals: Bacterial cellulose (BC) dispersion with a fiber content of ~0.7 wt.% was kindly provided by Ms. C.Y. Zhong (Hainan Yeguo Foods Co., Ltd., Hainan, China). Other chemicals such as 2,2,6,6-tetramethylpiperidine-1-oxyl radical (TEMPO), NaBr, NaOH, HCl, NaClO solution (6-14%) and tert-butyl alcohol (TBA) were purchased from Aladdin, which were directly used without further purification. All the water used in current work was milli-Q water.

Synthesis of TOBC: Firstly, TEMPO (0.10 mmol, 0.016 g) and NaBr (0.97 mmol, 0.1 g) were mixed in water (100 mL) under stirring for 1 h. Then the BC dispersion (25 mL, 14 mg BC) was added into above solution. After that, the reaction was triggered by introducing 6-14 % NaClO solution (0.03 mmol, 2 mL) and concentrated HCl (0.07 mmol, 2 mL) at room temperature (RT). The pH value was adjusted to 10.0 by using 0.5 M NaOH at the end of the reaction. The resultant precipitation was collected by centrifugation, and washed by deionized water, followed by being dispersed in 25 mL of a 5:1 (v/v) water/TBA mixture, and stirring for 2 h to form a transparent suspension. Finally, the suspension was freeze-dried, leading to the formation of a white aerogel, which was referred to as sample TOBC.

Synthesis of TOBC-derived carbon aerogels: The as-prepared TOBC aerogel was pyrolyzed in a N_2 atmosphere at the desired temperatures of 700, 800 and 900 °C for 2 h, which were referred to as sample TOCF-*x* (*x* stands for the fixed pyrolysis temperature). For comparison, the BC-pyrolyzed carbon aerogel was prepared through the following process: the BC dispersion (25 mL) was added into 25 mL water under stirring for 2 h at RT, followed by freeze drying and pyrolysis at 800 °C for 2 h, which was referred to as sample CF. The TOBC-derived carbon aerogel without the addition of TBA was also prepared with the same procedure as that of sample CF, and the obtained product was referred to as OCF. The pyrolysis procedure for the samples were given in Fig. S2 in Supporting Information.

Characterizations: The products were characterized using a field emission scanning

electron microscope (FESEM, S-4800, Hitachi, Japan) and high-resolution transmission electron microscopy (HRTEM, JEM-2100F, JEOL, Japan). The carbon yield of different precursors was probed by thermogravimetric analysis (TGA, Germany). The phase compositions were studied by a X-ray powder diffraction (XRD, D8 Advance, Bruker, Germany) equipped with Cu-Kα radiation (λ = 1.5406 Å). The Raman spectra were recorded on the machine of Renishaw inVia (UK Raman spectrometer system). The surface species and chemical states were measured by XPS (ES-CALAB 250Xi, Thermo Fisher Scientific America). The N2-sorption isotherms were collected on Tristar II (Micrometrics, ASAP 2020 HD88, US) at 77 K. The pore size distribution (PSD) was obtained by Barrett-Joyner-Halenda (BJH) model using the adsorption branch of the isotherm. The compressive tests of all samples were carried out by an Instron 5565A testing machine. The strain ramp rate was maintained at 10 mm per min, and multiple cycle tests were set at 50 mm per min.

Electrochemical measurements: The cyclic voltammetry (CV), galvanostatic charge-discharge (GCD) and electrochemical impedance spectroscopy (EIS) curves of the samples were collected on an electrochemistry workstation (Autolab, PGSTAT302N, Switzerland) in a typical three-electrode system, with Pt foil as the counter electrode, a Ag|AgCl/KCl (3 M KCl saturated) as the reference electrode, and 6 M KOH aqueous solution as the electrolyte. A single piece of CF, OCF and TOCF with a size of 1.0 × 1.0 × 0.3 cm^3 was used as working electrode, and soaked in 6.0 M KOH for 2 h before use. The CV tests were performed within a potential window of –1~0 V at a scan rate from 5 to 100 mV s^{-1}. The GCD tests were evaluated at different current densities of 1–20 A g^{-1}. The EIS plots were recorded through the frequency range of 10000-0.01 Hz with a 10 mV sinusoidal voltage at open circuit potential. The specific capacitance of electrodes (C_s, F g^{-1}) was calculated from the discharge curves by:

$$Cs = \frac{I\,\Delta t}{m\,\Delta V} \quad \text{.....(1)}$$

where I (A) is the constant current, Δt (s) is the discharge time, ΔV (V) represents the absolute discharge potential window, and m (g) corresponds to the total mass of the carbon aerogel.

For the test in two-electrode system, a symmetrical two-electrode device was fabricated in 6 M KOH electrolyte, with a total mass for both working electrodes of ~3.6 mg. The specific capacitance of electrode (C_g, F g^{-1}), the energy density E (Wh kg^{-1}), power density P (W kg^{-1}) of the devices were calculated by following equations:

$$Cg = \frac{4I\Delta t}{m\,\Delta V} \quad \text{.....(2)}$$

$$E = \frac{C\,\Delta V^2}{2} \quad \text{..... (3)}$$

$$P = \frac{E}{\Delta t} \quad \text{.....(4)}$$

where I (A) is the constant current, Δt (s) is the discharge time, ΔV (V) refers to the absolute discharge potential window, m (g) responds to the total mass of the carbon aerogels, and C (F g^{-1}) represents the capacitance.

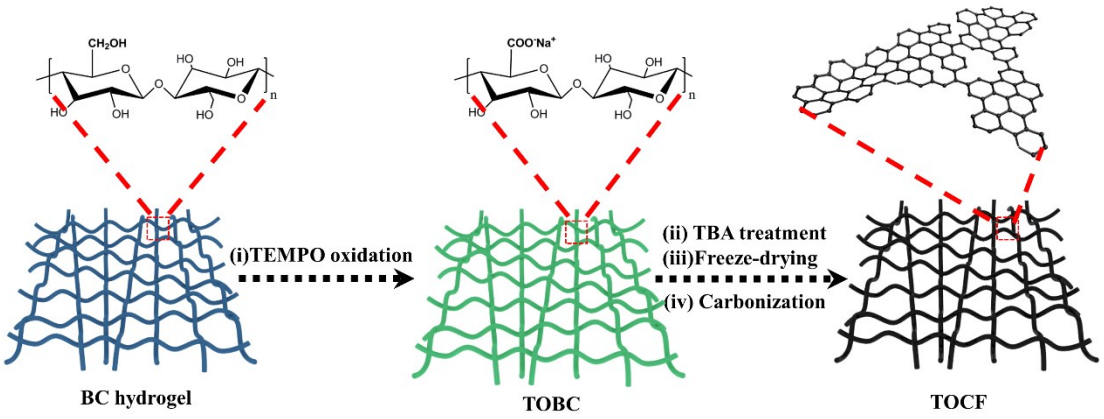

Fig. S1 Schematic illustration on the fabrication of carbon nanofiber aerogel.

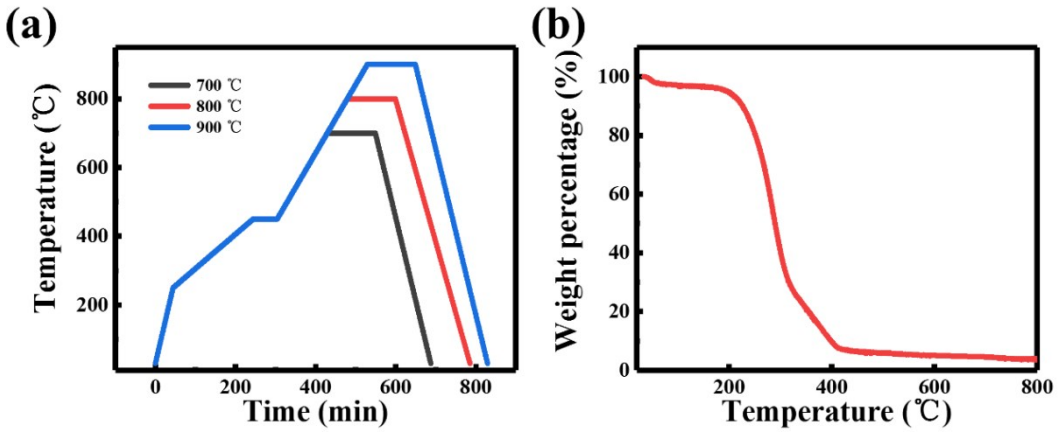

Fig. S2 (a) The used carbonization processes for samples CF-*x*, OCF-*x*, TOCF-*x* (*x* = 700, 800 and 900 °C). (b) TGA curves of sample TOCF-800.

Before 250 °C, the heating rate is set at 5 °C min^{-1}, considering the fact that fast heating rate have not significant effect on the formation of 3D network structure. It seems that the main weight loss is occurred between 250 and 450 °C (Fig. S2b). Accordingly, the heating rate is set as low as 1 °C min^{-1} below 450 °C. After that, the heating rate is slightly increased to 2 °C min^{-1} to make them be fully carbonized, and meanwhile maintain the 3D network structure well.

Fig. S3 Photographs of the as-prepared sample TOCF-800 weighting on an electronic balance, evidencing that the weight the sample is 6.14 mg. The diameter and height of sample TOCF-800 in cylinder configuration are 1.52 cm and 1.25 cm, respectively, demonstrating that its volume is ~2.27 cm^3. Accordingly, its density is *ca.* 2.7 mg cm^{-3}.

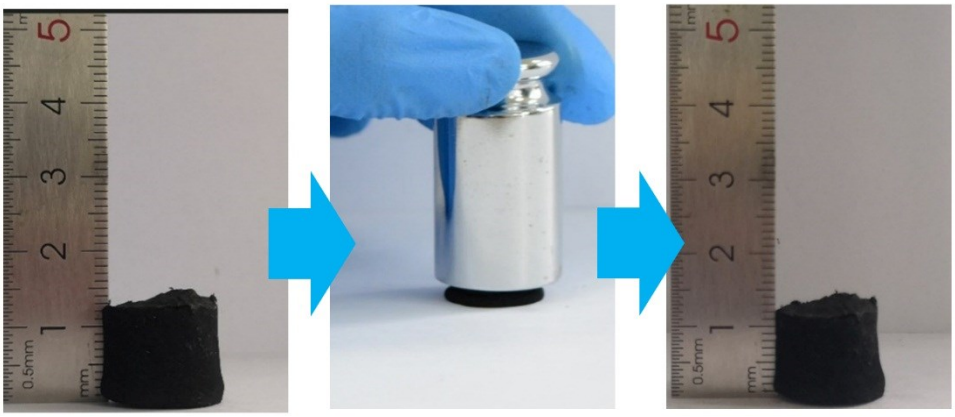

Fig. S4 The photographs to show one compression cycle over sample TOCF-800, representing its high flexibility.

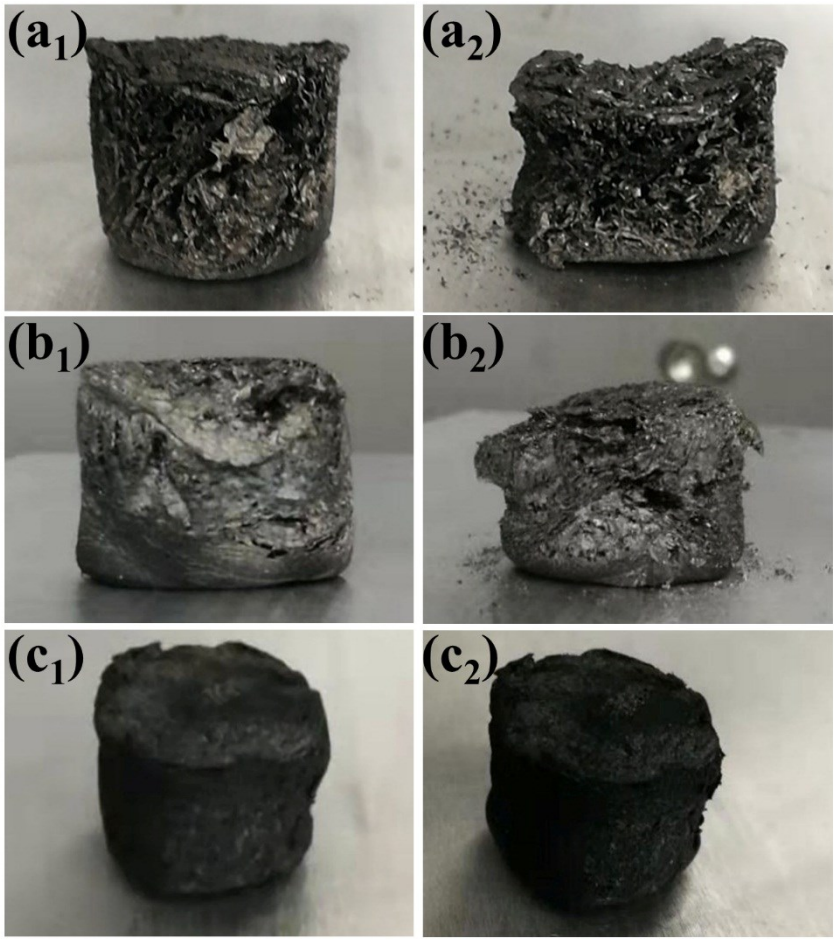

Fig. S5 The digital photos of: (a_1-a_2) Sample CF-800 before and after one compressive test, respectively. (b_1-b_2) Sample OCF-800 before and after 100th compressive tests, respectively. (c_1-c_2) Sample TOCF-800 before and after 100th compressive tests, respectively.

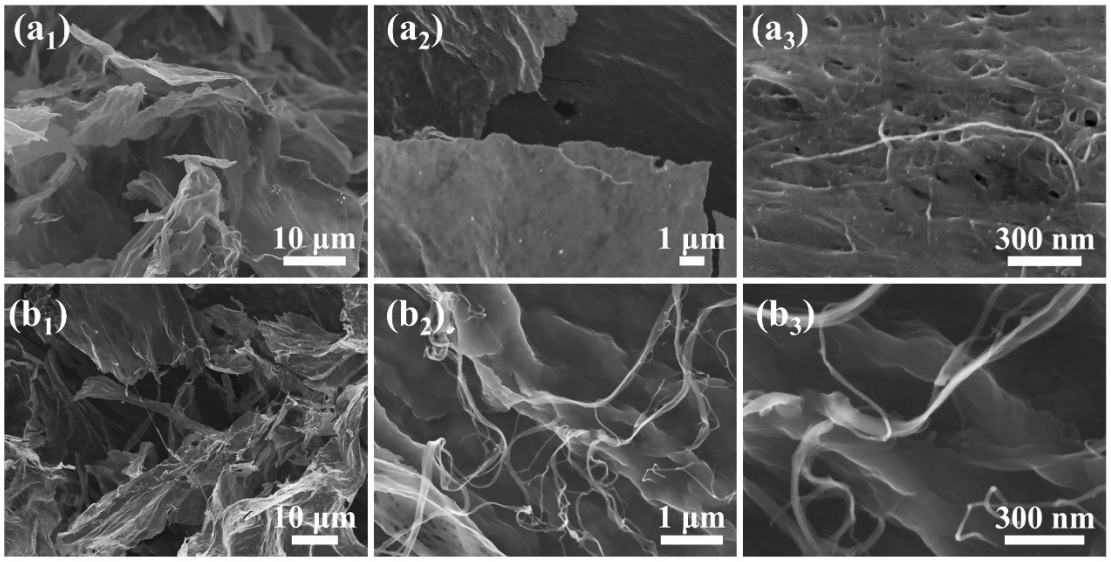

Fig. S6 (a_1-a_3) Typical SEM images of sample CF under different magnifications. (b_1-b_3) Typical SEM images of sample OCF under different magnifications.

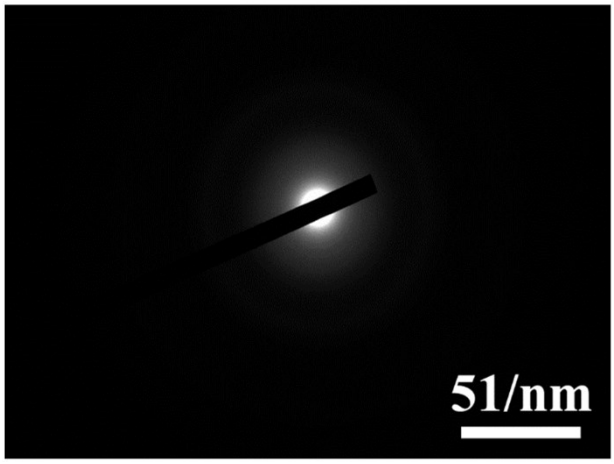

Fig. S7 The SAED pattern of sample TOCF-800, disclosing its amorphous nature.

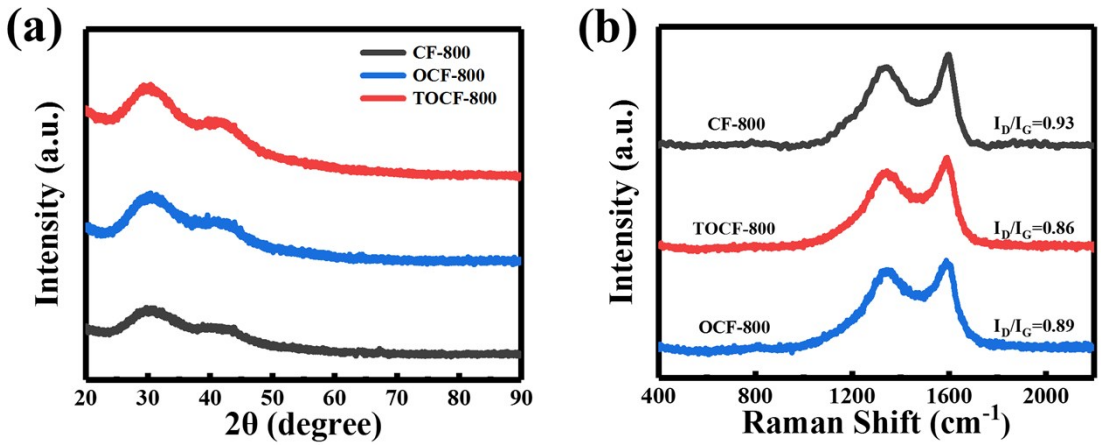

Fig. S8 (a-b) The representative XRD patterns and Raman spectra of samples CF, OCF and TOCF, respectively.

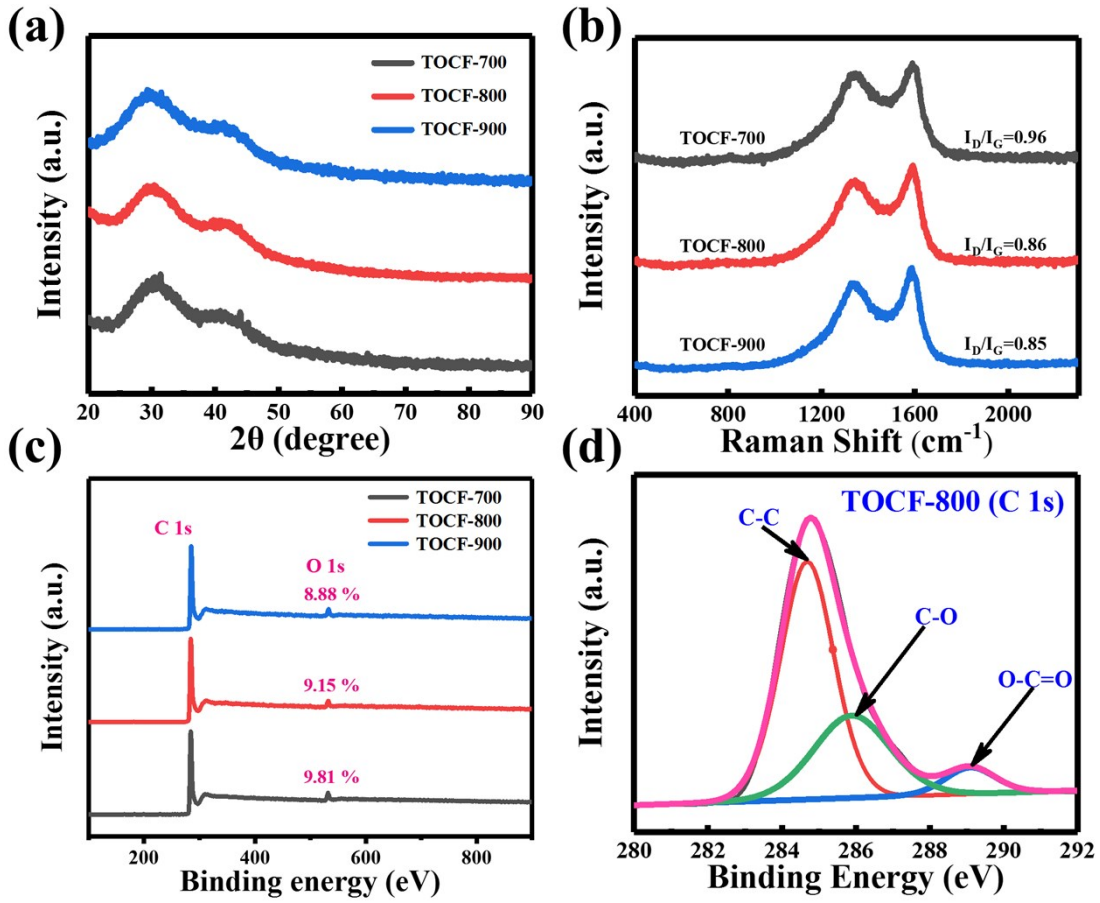

Fig. S9 (a-c) XRD patterns, Raman spectra, and XPS survey spectra of samples TOCF-*x* (*x* = 700, 800 and 900 °C), respectively. (d) The high-resolution C1s spectra of sample TOCF-800.

It is known that carbonization temperature is vital for the growth of TOBC-derived carbon aerogels. It is disclosed that the XRD patterns of samples TOCF-*x* (*x* = 700, 800 and 900 °C) are similar (Fig. S9a) However, with the increase of the fixed carbonization temperatures, the intensity of the peak at 43° gradually increases, suggesting the slight increase of graphitization degrees. Such similar result can also be observed from the recorded Raman spectra, where I_D/I_G ratios decrease from 0.96 to 0.85, with the rise of the temperatures from 700 to 900 °C. Based on the XPS analyses, it suggests that, as the increase of the fixed pyrolysis temperatures, the resultant carbon aerogels exhibit a decrease trend of O contents from 9.81, 9.15 to 8.88%, which verifies the enhanced crystallinity with the increase of the applied carbonization temperatures.

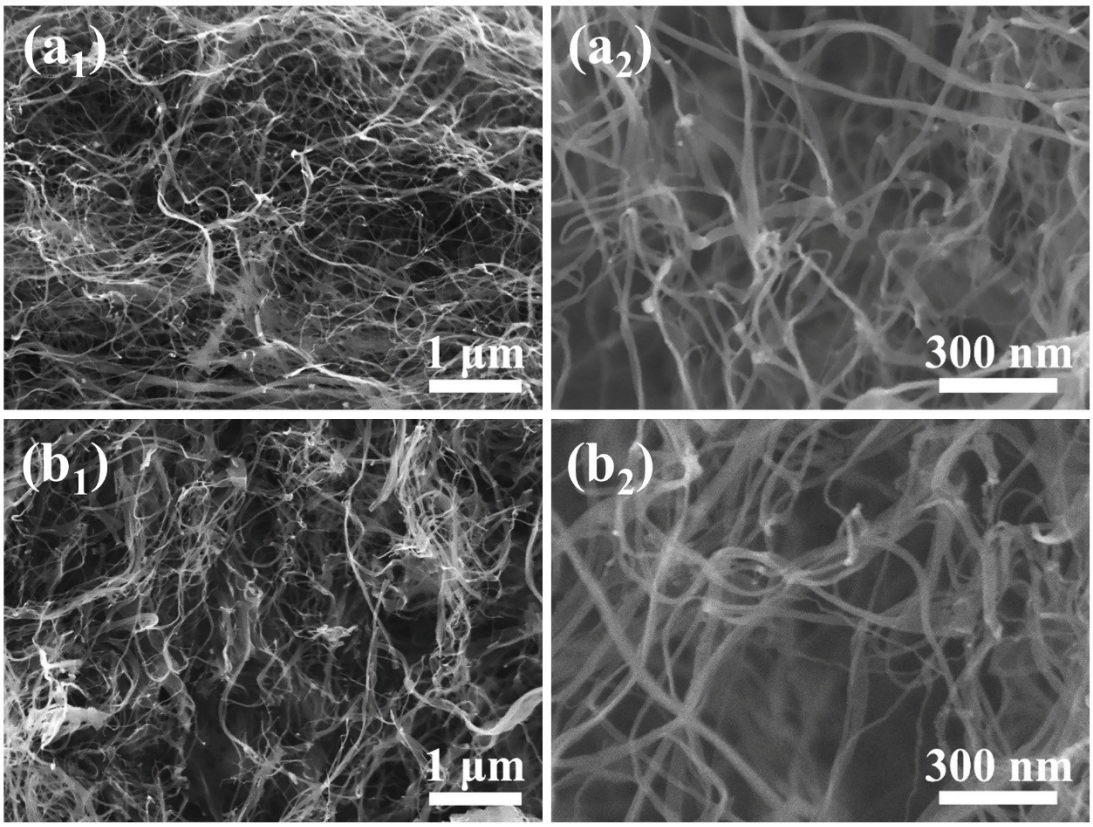

Fig. S10 (a_1-a_2) Typical SEM images of sample TOCF-700 under different magnifications. (b_1-b_2) Typical SEM images of sample TOCF-900 under different magnifications.

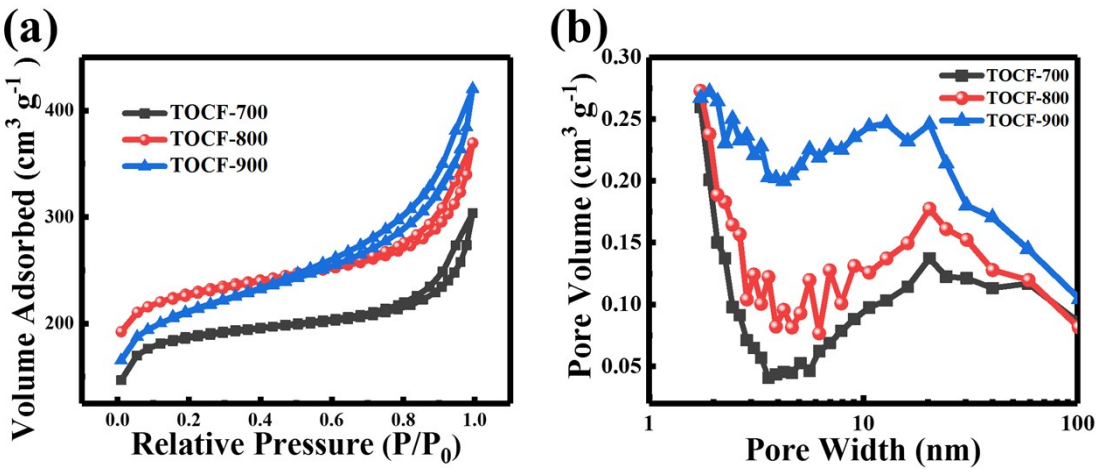

Fig. S11 (a-b) N_2 adsorption-desorption isotherms and pore size distributions of samples TOCF-*x* (*x* = 700, 800 and 900 °C).

As shown in Fig. S11a, the SSA values of sample TOCF-800 (712 m^2 g^{-1}) is higher than those of sample TOCF-700 (584 m^2 g^{-1}) and TOCF-900 (674 m^2 g^{-1}), all of which are comparable with those of graphene-based aerogels.[1,2] As disclosed by the pore size distributions (Fig. S11b), sample TOCF-800 presents sharp peaks at ~1.9, 3.1, 3.6, 4.3, 5.6, 6.9, 9.1 and 20.3 nm, indicating the coexistence of hierarchical micropores and mesopores within this aerogel. These experimental results confirm that the applied carbonization temperature profoundly influences the oxygen-involving defect, specific surface area and pore distribution of the as-fabricated carbon aerogels.

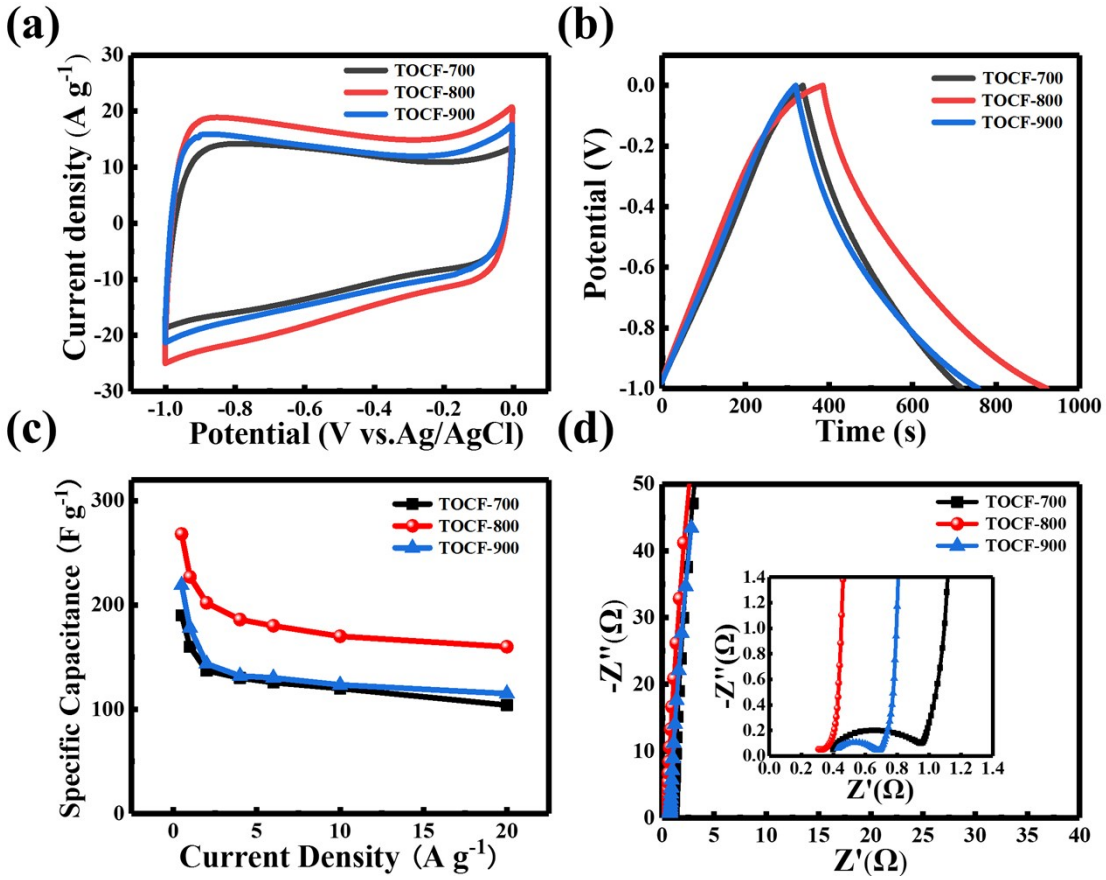

Fig. S12 Electrochemical performance of samples TOCF-*x* (*x* = 700, 800 and 900 °C) in three-electrode system using 6 M KOH as the electrodes: (a) CV plots at 100 mV s^{-1}, (b) GCD curves at 0.5 A g^{-1}, (c) specific capacitances at different current densities, and (d) Nyquist plots.

All the CV curves of samples TOCF-*x* present a similar near-rectangular shape at a high scan rate of 100 mV s^{-1}, indicating their typical capacitive behavior with a small internal resistance.[3] The slightly larger CV enclosure area of sample TOCF-800 than the other two counterparts implies a higher specific surface area with a higher specific capacitance. Their typical GCD curves at a current density of 0.5 A g^{-1} (Fig. S12b) reveal the triangular and symmetric charge-discharge curves with small voltage drop, suggesting a small overall resistance. The longer discharge time of TOCF-800 indicates a higher C_s, in accordance with CV tests. Particularly, the TOCF-800 electrode possesses a high capacitance of 268 F g^{-1} at the current density of 0.5 A g^{-1}, which is higher than samples TOCF-700 (190 F g^{-1}) and TOCF-900 (219 F g^{-1}) (Fig. S12c). As shown by the EIS data (Figure S10d), sample TOCF-800 exhibits a lower *Rct* value (0.29 Ω) than samples TOCF-700 (1.9 Ω) and TOCF-900 (0.66 Ω) counterparts.

Furthermore, the equivalent series resistance (ESR) of sample TOCF-800 electrode is evaluated to be ~0.27 Ω, lower than those of samples TOCF-700 (0.41 Ω) and TOCF-900 (0.34 Ω). Briefly, sample TOCF-800 has the lowest charge transfer resistance and internal resistance.[4]

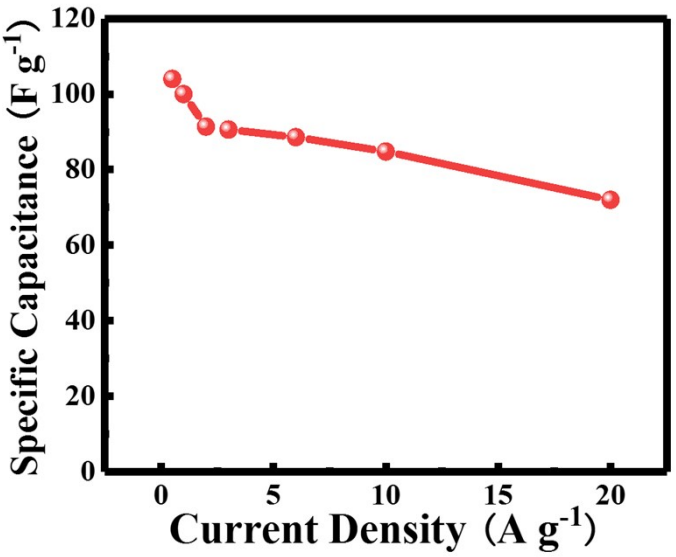

Fig. S13 The recorded specific capacitances at different current densities of the as-constructed SSSCs based on sample TOCF-800.

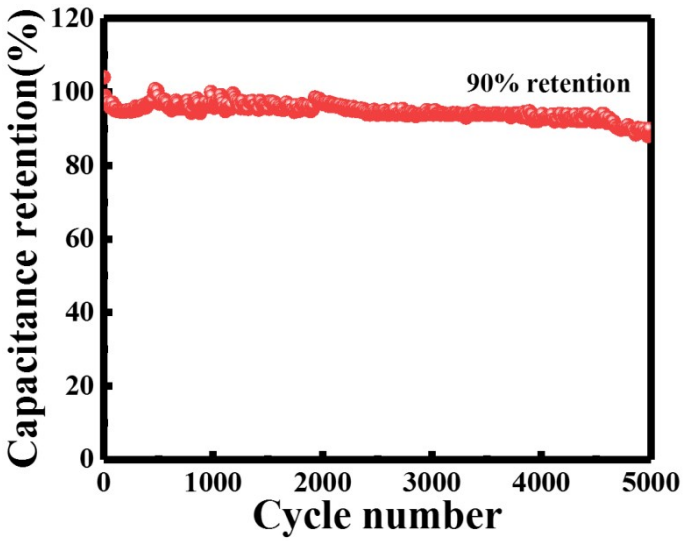

Fig. S14 Cycling stability at a density of 3 A g^{-1} over 5000 cycles of the SSSCs based on sample TOCF-800.

Table S1. Comparison on the densities and mechanical properties among typically reported carbon aerogels and those in this work.

Building blocks	Density (mg cm^{-3})	Compressibility (%)	Cycles (strain)	Plastic deformation	Rf.
Poplars catkin	4.3	80	100 (50%)	~18%	5
RGO/ lignin	12	70	10 (50%)	Above 5%	6
Graphene	6.9	80	100 (50%)	Above 10%	7
Electrospun Nanofibers	9.6	~82	100 (60%)	4.8%	8
Carbon nanotubes	5-10	100	100 (60%)	~17.5%	9
3D Printed Graphene	53	38	10 (50%)	~15%	10
Ni Micro Lattices	14	~70%	10 (50%)	3%	11
TOCF	**2.7**	**Above 90**	**100 (90%)**	**~3%**	**This Work**

Table S2. Comparison on the specific capacitances of the typically reported electrode of SCs based on carbon aerogels.

Electrode material	Test condition	C_s (F/g)	Electrolyte	Test method	Rf.
BC	1 A g^{-1}	37	1M H_2SO_4	self-supporting	12
CNF/GN	1 A g^{-1}	215	1M H_2SO_4	self-supporting	12
Layer-structured graphene paper	1 mV s^{-1}	142	1 M H_2SO_4	self-supporting	13
Graphene aerogels	1 mV s^{-1}	181	1 M H_2SO_4	self-supporting	13
Wood-NFC derived CNFs	1 A g^{-1}	68	2.0 M H_2SO_4	carbon cloth	14
BC@SiO_2 membrane derived CN-BC	0.5 A g^{-1}	302	6 M KOH	self-supporting	15
Sugarcane bagasse derived carbon materials	2 mV s^{-1}	88	6 M KOH	nickel foil	16
Resorcinol–formaldehyde gel	1 mV s^{-1}	110.06	6 M KOH	nickel foil	17
TOCF	**0.5 A g^{-1}**	**268**	**6 M KOH**	**self-supporting**	**This work**

Table S3. Comparison on the cycling stabilities of typically reported SCs based on biomass-derived carbon electrodes.

Electrode materials	Current density ($A\ g^{-1}$)	Cycles	Retention (%)	Rf.
BC-derived N,P nanowires	100mV/s	6000	87	18
Wood-NFC derived CNFs	8	10000	98	14
BC@SiO_2 membrane derived CN-BC	2	5000	97	15
Sugarcane bagasse derived carbon material	1	5000	93.86	16
Porous CNFs	1	5000	88	19
Ppy@TOBC/rGo	1	5000	79	20
A-p-BC-N	2	5000	95.9	21
Jujube -derived carbon sample	10	10000	91	22
Chitosan derived carbon aerogel	1	10000	92.1	23
Glucose-derived carbon/carbon nanotube	1	10000	75	24
TOCF	**1**	**10000**	**98**	**This work**

Table S4. Comparison on the capacitive performances of typically reported SSSCs based on carbon electrodes.

Electrode materials	Range	Rate capability (%)	Supporting substrate	Rf.
V_3S_4 /graphene//MnO_2 /graphene	From 10 to 200 mV s^{-1}	38.2	self-supporting	25
Co_3O_4//carbon aerogel	From 1 to 10 A g^{-1}	58	nickel foil	26
MnO_2 –GO foam	From 1 to 10 A g^{-1}	54.2	Ni foam	27
Carbon aerogel derived from bagasse	From 2 to 50 mV s^{-1}	56.8	nickel foil	16
CNT/MoO_{3-x}	From 0.133 to 0.13 A cm^{-3}	63.3	self-supporting	28
MoS_2-rGO/MWCNT	From 0.07 to 2 A cm^{-3}	60.3	self-supporting	29
porous graphene on carbon cloth	From 5 to 100 mV s^{-1}	62.7	self-supporting	30
CNT/PANI	From 1 to 5 mA cm^{-2}	65	self-supporting	31
Graphene-based carbon aerogel	From 0.2 to 10 A g^{-1}	54.8	nickel foil	3
N-doped porous carbon nanofibers	From 0.5 to 8 A g^{-1}	54	self-supporting	32
TOCF	**From 0.5 to 20 A g^{-1}**	**69.2**	**self-supporting**	**This work**

Table S5. Comparison on the cycling stabilities of typically reported SSSCs based on carbon electrodes.

Electrode materials	Current density	Cycles	Retention (%)	Ref.
Co_3O_4//carbon aerogel	2 A g^{-1}	1000	85	26
PPy-MnO2-CF	1 A cm^{-3}	1000	86.7	33
CFP/PPy// RGO/MWCNT	1 A g^{-1}	2000	93	34
Ni/MnO_2//Ni/active carbon	5 mV s^{-1}	1000	85.1	35
MnO_2 Covered $FeCo_2O_4$	5 mA cm^{-2}	1500	94	36
porous CNT/PANI hydrogel film	0.5 A g^{-1}	1500	92	37
PANI/CNT	1 A g^{-1}	1000	91.9	38
NPG-PPy	4.4 A g^{-1}	900	78	39
Co_9S_8 // Co_3O_4 @RuO 2	10 A g^{-1}	2000	90.2	40
GQDs//PANI	1 V s^{-1}	1500	85.6	41
TOCF	**3 A g^{-1}**	**5000**	**90**	**This work**

REFERENCES

1 X. N. Tang, C. Z. Liu, X. R. Chen, Y. Q. Deng, X. H. Chen, J. J. Shao and Q. H. Yang, Carbon, 2019, **146**, 147-154.

2 Y. Huang, F. Lai, L. Zhang, H. Lu, Y. E. Miao and T. Liu, Sci. Rep., 2016, **6**, 31541.

3 D. Shan, J. Yang, W. Liu, J. Yan and Z. Fan, J. Mater. Chem. A., 2016, **4**, 13589-13602.

4 G. Wang, L. Zhang and J. Zhang, Chem. Soc. Rev., 2012, **41**, 797.

5 L. Li, T. Hu, H. Sun, J. Zhang and A. Wang, ACS Appl. Mater. Inter., 2017, **9**, 18001-18007.

6 Z. Zeng, C. Wang, Y. Zhang, P. Wang, S. I. Seyed Shahabadi, Y. Pei, M. Chen and X. Lu, ACS Appl. Mater. Inter., 2018, **10**, 8205-8213.

7 J. Li, J. Li, H. Meng, S. Xie, B. Zhang, L. Li, H. Ma, J. Zhang and M. Yu, J. Mater. Chem. A., 2013, **2**, 2934-2941.

8 Y. Si, J. Yu, X. Tang, J. Ge and B. Ding, Nat. Commun., 2014, **5**, 5802.

9 X. Gui, J. Wei, K. Wang, A. Cao, H. Zhu, Y. Jia, Q. Shu and D. Wu, Adv. Mater., 2010, **22**, 617-621.

10 C. Zhu, T. Y. Han, E. B. Duoss, A. M. Golobic, J. D. Kuntz, C. M. Spadaccini and M. A. Worsley, Nat. Commun., 2015, **6**, 6962.

11 T. A. Schaedle, A. J. Jacobsen, A. Torrents, A. E. Sorensen, J. Lian, J. R. Greer, L. Valdevit and W. B. Carter, Science, 2011, **334**, 962-965.

12 H. Luo, P. Xiong, J. Xie, Z. Yang, Y. Huang, J. Hu, Y. Wan and Y. Xu, Adv. Funct. Mater., 2018, **28**, 1803075.

13 Z. S. Wu, A. Winter, L. Chen, Y. Sun, A. Turchanin, X. Feng and K. Mullen, Adv. Mater., 2012, **24**, 5130-5135.

14 S. C. Li, B. C. Hu, Y. W. Ding, H. W. Liang, C. Li, Z. Y. Yu, Z. Y. Wu, W. S. Chen and S. H. Yu, Angew. Chem. Int. Edit., 2018, **57**, 7085-7090.

15 X. Hao, J. Wang, B. Ding, Y. Wang, Z. Chang, H. Dou and X. Zhang, J. Power Sources., 2017, **352**, 34-41.

16 P. Hao, Z. Zhao, J. Tian, H. Li, Y. Sang, G. Yu, H. Cai, H. Liu, C. P. Wong and A.

Umar, Nanoscale, 2014, **6**, 12120-12129.

17 J. Li, X. Wang, Q. Huang, S. Gamboa and P. J. Sebastian, J. Power Sources., 2006, **158**, 784-788.

18 Z. Hu, S. Li, P. Cheng, W. Yu, R. Li, X. Shao, W. Lin and D. Yuan, J. Mater. Sci., 2015, **51**, 2627-2633.

19 L. Zhang, Y. Jiang, L. Wang, C. Zhang and S. Liu, Electrochim. Acta., 2016, **196**, 189-196.

20 N. Sheng, S. Chen, J. Yao, F. Guan, M. Zhang, B. Wang, Z. Wu, P. Ji and H. Wang, Chem. Eng. J., 2019, **368**, 1022-1032.

21 L. F. Chen, Z. H. Huang, H. W. Liang, W. T. Yao, Z. Y. Yu and S. H. Yu, Energy Environ. Sci., 2013, **6**, 3331.

22 X. Liu, C. Ma, J. Li, B. Zielinska, R. J. Kalenczuk, X. Chen, P. K. Chu, T. Tang and E. Mijowska, J. Power Sources., 2019, **412**, 1-9.

23 P. Hao, Z. Zhao, Y. Leng, J. Tian, Y. Sang, R. I. Boughton, C. P. Wong, H. Liu and B. Yang, Nano Energy, 2015, **15**, 9-23.

24 N. Rey Raap, M. Enterria, J. I. Martins, M. F. R. Pereira and J. L. Figueiredo, ACS Appl. Mater. Inter., 2019, **11**, 6066-6077.

25 T. Zhai, X. Lu, H. Wang, G. Wang, T. Mathis, T. Liu, C. Li, Y. Tong and Y. Li, Nano Lett., 2015, **15**, 3189-3194.

26 W. Liu, X. Li, M. Zhu and X. He, J. Power Sources., 2015, **282**, 179-186.

27 Z. Zhang, F. Xiao, L. Qian, J. Xiao, S. Wang and Y. Liu, Adv. Energy Mater., 2014, **4**, 1400064.

28 X. Xiao, T. Li, Z. Peng, H. Jin, Q. Zhong, Q. Hu, B. Yao, Q. Luo, C. Zhang, L. Gong, J. Chen, Y. Gogotsi and J. Zhou, Nano Energy, 2014, **6**, 1-9.

29 G. Sun, X. Zhang, R. Lin, J. Yang, H. Zhang and P. Chen, Angew. Chem. Int. Edit., 2015, **54**, 4651-4656.

30 S. Wang, B. Pei, X. Zhao and R. A. W. Dryfe, Nano Energy, 2013, **2**, 530-536.

31 S. Zeng, H. Chen, F. Cai, Y. Kang, M. Chen and Q. Li, J. Mater. Chem. A., 2015, **3**, 23864-23870.

32 F. Miao, C. Shao, X. Li, K. Wang and Y. Liu, J. Mater. Chem. A., 2016, **4**, 4180-

4187.

33 J. Tao, N. Liu, W. Ma, L. Ding, L. Li, J. Su and Y. Gao, Sci. Rep., 2013, **3**, 2286.

34 C. Yang, J. Shen, C. Wang, H. Fei, H. Bao and G. Wang, J. Mater. Chem. A., 2014, **2**, 1458-1464.

35 L. Zhang, P. Zhu, F. Zhou, W. Zeng, H. Su, G. Li, J. Gao, R. Sun and C. P. Wong, ACS Nano, 2016, **10**, 1273-1282.

36 B. Zhu, S. Tang, S. Vongehr, H. Xie and X. Meng, ACS Appl. Mater. Inter., 2016, **8**, 4762-4770.

37 X. Xiang, W. Zhang, Z. Yang, Y. Zhang, H. Zhang, H. Zhang, H. Guo, X. Zhang and Q. Li, RSC Adv., 2016, **6**, 24946-24951.

38 C. Meng, C. Liu, L. Chen, C. Hu and S. Fan, Nano Lett., 2010, **10**, 4025-4031.

39 F. Meng and Y. Ding, Adv. Mater., 2011, **23**, 4098-4102.

40 J. Xu, Q. F. Wang, X. W. Wang, Q. Y. Xiang, B. Liang, D. Chen and G. Z. Shen, ACS Nano, 2013, **7**, 5453–5462.

41 W. Liu, X. Yan, J. Chen, Y. Feng and Q. Xue, Nanoscale, 2013, **5**, 6053-6062